

Observation of autoionization dynamics and sub-cycle quantum beating in electronic molecular wave packets

M. Reduzzi^{1,3}, W.-C. Chu², C. Feng¹, A. Dubrouil¹,
J. Hummert¹, F. Calegari³, F. Frassetto⁴, L. Poletto⁴,
O. Kornilov⁵, M. Nisoli^{1,3}, C.-D. Lin², G. Sansone^{1,3}

(1) Dipartimento di Fisica, Politecnico Piazza Leonardo da Vinci 32, 20133 Milano Italy

(2) Physics Department, Kansas State University, Manhattan, Kansas 66506, U.S.A.

(3) Institute of Photonics and Nanotechnologies, CNR Politecnico, Piazza Leonardo da Vinci 32, 20133 Milano Italy

(4) Institute of Photonics and Nanotechnologies, CNR via Trasea 7, 35131 Padova Italy

(5) Max-Born-Institut, Max Born Strasse 2A, D-12489 Berlin

email: giuseppe.sansone@polimi.it

Abstract. The coherent interaction with ultrashort light pulses is a powerful strategy for monitoring and controlling the dynamics of wave packets in all states of matter. As light presents an oscillation period of a few femtoseconds ($T = 2.6$ fs in the near infrared spectral range), the fundamental light-matter interaction occurs on the sub-cycle timescale, i.e. in a few hundred attoseconds. In this work, we resolve the dynamics of autoionizing states on the femtosecond timescale and observe the sub-cycle evolution of a coherent electronic wave packet in a diatomic molecule, exploiting a tunable ultrashort extreme ultraviolet pulse and a synchronized infrared field. The experimental observations are based on measuring the variations of the extreme ultraviolet radiation transmitted through the molecular gas. The different mechanisms contributing to the wave packet dynamics are investigated through theoretical simulations and a simple three level model. The method is general and can be extended to the investigation of more complex systems.

1. Introduction

Controlling the motion of electrons in a molecule during the unfolding of a chemical process is one of the main goals of attosecond science [1, 2, 3]. As chemical bonds are associated with the (multi-)electronic wavefunction distribution, the possibility to observe and steer the electronic motion in real-time with field-controlled pulses opens new perspectives in the manipulation of chemical reactivity. This novel approach for molecular quantum control is at the heart of the expanding field of attosecond chemistry and it is attracting an increasing number of theoretical and experimental efforts [4, 5]. Electron molecular dynamics is initiated with the creation of an electronic wave packet. Using an extreme ultraviolet (XUV) attosecond pulse, wave packets comprising bound and continuum states can be excited [6]. The subsequent ultrafast dynamics can be observed by processes such as charge rearrangement on a timescale of few tens of attoseconds [7], or by the oscillation of the charge cloud over the entire molecular structure on a timescale of few femtoseconds [8]. For longer timescales, the nuclear motion comes into play calling for the coupled description of the electronic and nuclear degrees of freedom [9].

In 2010, the first experimental demonstration of the attosecond control of the electronic motion in a dissociating molecule (hydrogen and deuterium) was reported, measuring the emission direction of the ionic fragments resulting from molecular dissociation [10]. Photoelectron and photoion spectroscopy, however, are based on the ionization (and dissociation) of the molecular system, implying photoionization as the initial trigger of the molecular dynamics. The creation and manipulation of bound electronic states in the neutral molecule are of extreme interest for chemical reactivity control, pointing out the need of a general experimental technique to access the dynamics of bound states.

In this context, it is important to point out that the excitation of an electronic wave packet corresponds to the creation of a time-dependent electronic charge distribution, and therefore to a dipole moment $d(t)$. An initial study of the dipole in neutral molecules induced by an intense laser pulse and measured by a time-delayed ionizing XUV pulse was reported recently [11]. A more direct method for gaining insight in the dynamics of the system is the spectral characterization of the induced radiation. In this picture, the initial attosecond pulse creates a coherent population of states, triggering the polarization of the medium. The dynamics occurring after the excitation pulse is encoded in the time-dependent polarization and, therefore, in the spectral amplitude and phase of the radiation transmitted through the system, giving access to the evolution of the electronic states. This technique, usually named attosecond transient absorption spectroscopy, has been applied for the investigation of noble gas atoms, gaining access to the evolution of singly excited states in helium [12, 13, 14, 15] and neon [16], and doubly excited states in argon [17] and helium [18, 19, 20].

Attosecond broadband wave packets spanning across the ionization threshold have also been studied in time-delayed photoelectron measurement [6]; however, the

bound state part of the wave packet could be revealed only indirectly in the electron measurement.

In this work, we apply attosecond transient absorption to a molecular system, demonstrating the creation of a complex electronic wave packet composed of bound excited states and autoionizing resonances. Using a synchronized infrared (IR), carrier-envelope-phase (CEP) stable field, the evolution of the wave packet can be observed in time. By measuring the broadband XUV absorption cross section vs the IR time delay, we extract information on the autoionization dynamics and on the population redistributions in the different final states of the molecule.

2. Three-level model

In order to illustrate the excitation of the electronic wave packets and observation of the time delay dependent patterns in the transmitted spectra, we consider a three level system interacting with a broadband XUV pulse and a synchronized CEP-stable IR field. In spite of its simplicity, the model allows one to gain a simple, intuitive picture of the experimental results and simulations, pointing out the generality of the approach. The population, initially in the ground state ψ_0 , is raised (at the instant $t = 0$) to two excited states ψ_1 and ψ_2 by interaction with an attosecond XUV pulse creating a coherent wave packet (see Fig. 1):

$$\psi(t) = c_2(t)e^{[-i(E_2/\hbar - i\Gamma_2/2)t]}\psi_2 + c_1(t)e^{[-i(E_1/\hbar - i\Gamma_1/2)t]}\psi_1 + c_0(t)e^{[-iE_0t/\hbar]}\psi_0 \quad (1)$$

where $c_0(t)$, $c_1(t)$, and $c_2(t)$ are the time-dependent amplitudes of the ground, the first, and second excited state, characterized by energy E_0 , E_1 , and E_2 , respectively. We assume that the first and second excited states decay with time constants $1/\Gamma_1$ and $1/\Gamma_2$, respectively.

The attosecond pulse sets in a dipole oscillation $d(t)$, which is given by the sum of two contributions related to the coherent evolution of the states ψ_0, ψ_1 and ψ_0, ψ_2 (assuming no direct coupling between the two excited states): $d(t) = x_1(t) + x_2(t)$. The oscillation in time of the dipole moment (shown in Fig. 1a,b,c) is a direct manifestation of the coherent evolution of the molecular electronic charge associated to the three states. The fast modulations are due to the energy differences $E_1 - E_0$ and $E_2 - E_0$, while the slow variation of the amplitude is connected to the beating of the two dipoles with energy difference $E_2 - E_1$. The microscopic dipole moment determines a macroscopic polarization of the medium that affects both the phase (dispersion) and intensity (absorption/emission) of the XUV pulse transmitted through the medium. Information about the dynamical evolution of the system are, therefore, encoded in the spectral phase and amplitude of this radiation.

In the temporal domain, a perturbation of the freely-evolving dipoles, such as the interaction with a moderately intense IR pulse, will influence the evolution of the complex coefficients $c_1(t)$ and $c_2(t)$, thus leading to modifications in the oscillating dipoles. In Fig. 1 we consider (in the framework of the time-dependent perturbation

theory) the interaction of the three level system with a few-cycle IR pulse arriving at a delay $t = 20$ fs after the initial excitation. Before the arrival of the IR pulse, the dipole oscillation with (red line) and without (black line) IR laser field are indistinguishable, as shown in Fig. 1a. Around the delay $t = 20$ fs (Fig. 1b), the IR field (black dotted line) modifies the oscillations with respect to the unperturbed case. In terms of oscillating dipoles, the action of the IR field will depend on the relative phase between the electric field oscillations and the beating between the two dipoles at frequency $(E_2 - E_0)/\hbar$ and $(E_1 - E_0)/\hbar$. The modifications of the dipole oscillations remain encoded after the end of the IR pulse as shown in Fig. 1c.

In the spectral domain, the perturbation induced by the IR field leads to variations of the radiation transmitted through the sample (enhanced or reduced absorption or emission, and dispersion of the XUV light) as shown in Fig. 1d. The amplitudes $c_1(t)$ and $c_2(t)$ and also the populations of the excited states are modified sub-cycle by the IR field as shown in Fig. 1e. Due to the coherence between the ground state and the excited states the dipole oscillations can then be used as a reference to monitor the coupling between the states ψ_1 and ψ_2 induced by the IR field.

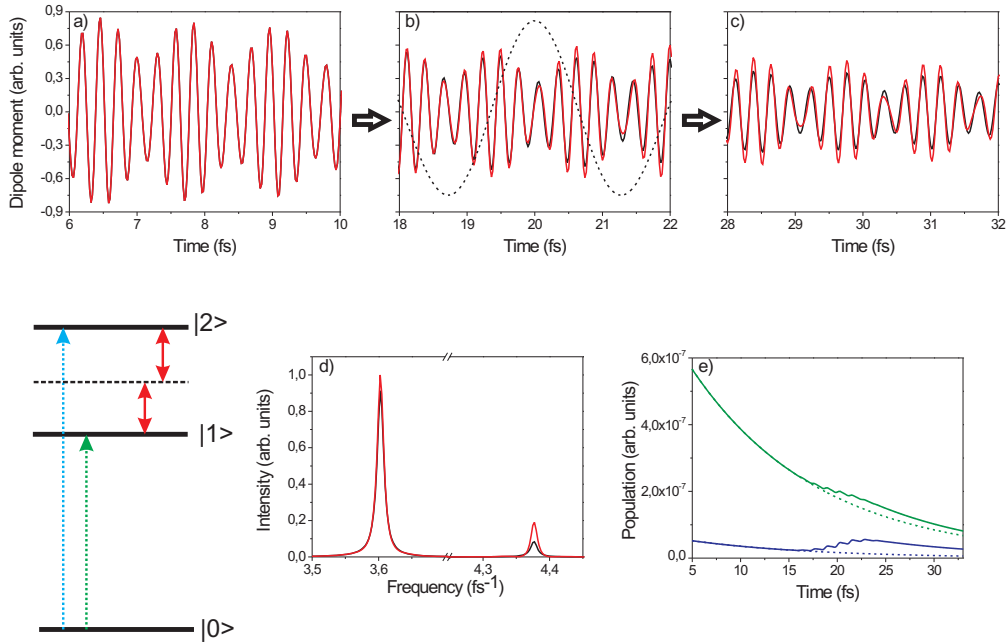


Figure 1. Dipole oscillations for three time intervals [6-10 fs] (a), [18-22 fs](b), and [28-32 fs](c) without (black line) and with IR field (red line). The pulse (black dotted line) arrives at a delay $t=20$ fs, with respect to the initial XUV excitation.(d) Fourier transform of the dipole moment without (black line) and with (red line) IR field .(e) Population of the upper (blue) and lower (green) excited states without (dashed lines) and with (solid lines) IR field. In the simulation a two-photon coupling between the excited states was considered.

In spite of its simplicity the three-state model allows one to describe several general aspects of the physical mechanism occurring in the interaction of an XUV pulse

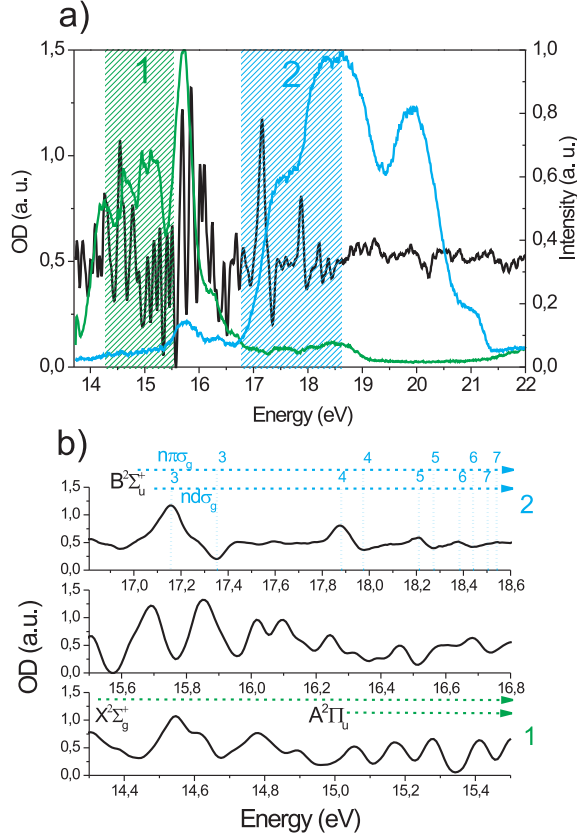


Figure 2. a) Nitrogen optical density in the XUV spectral region (left axis, black line) measured using the XUV radiation generated by high-harmonic radiation in xenon. Normalized spectral intensity of the XUV radiation generated in xenon and transmitted through a 150-nm-thick indium (green curve) or tin (blue curve) filter (right axis). The relevant energy ranges are indicated by green (bound states) and blue (Fano resonances) lines. b) Enlarged view of the measured nitrogen optical density. The blue lines (upper panel) indicate the position of the levels, characterized by quantum number n , belonging to the two series of Fano resonances (Hopfield absorption and apparent emission). The green lines (lower panel) indicate the energy region of features corresponding to excited levels converging to the ground ($X^2\Sigma_g^+$) and first excited state ($A^2\Pi_u$) of N_2^+ , respectively.

and a synchronized IR field with simple (atoms) and more complex systems (molecules).

In our experiment, we have investigated the electronic dynamics occurring in nitrogen after the creation of a broadband wave packet using different attosecond pulses. Differently from the simple three-state model, the cross-section of nitrogen in the vacuum ultraviolet region (14-22 eV) is characterized by several features corresponding to the excitation of the neutral molecule and of the molecular ion, as shown in Figs. 2a,b.

In order to quantify the absorption the nitrogen sample, we introduce the optical density defined as:

$$OD(\omega) = -\ln \left[\frac{S(\omega)}{S_0} \right] \quad (2)$$

where $S(\omega)$ is the XUV spectrum transmitted through the sample and $S_0(\omega)$ is the reference spectrum acquired without nitrogen. The radiation transmitted through the 3-mm-thick gas cell was analyzed using an XUV spectrometer composed of a toroidal mirror and a concave grating, which disperses the XUV light in the focal plane where a MCP coupled to a phosphor screen was placed. A CCD camera acquired the signal at the back of the phosphor screen. The design of the spectrometer ensures a high spectral resolution in the range 15-25 eV ($\Delta E = 30$ meV) that allows us to partially resolve the rich level structure of nitrogen in the 14-22 eV energy range.

The features visible in Fig. 2a are attributed to the Rydberg series converging to the ground ionic state ($X^2\Sigma_g^+$; $I_p = 15.58$ eV) and to the first ($A^2\Pi_u$; $E = 16.94$ eV) and second ($B^2\Sigma_u^+$; $E = 18.75$ eV) ionic excited states.

The energy region 16.8-18.6 eV (Fig. 2b upper panel) is characterized by features corresponding to the Hopfield absorption and apparent emission series [21]. These series correspond to two series of Fano(-Beutler) autoionizing resonances converging to the $B^2\Sigma_u^+$ excited ionic state. The Hopfield absorption and emission series have been attributed to the excitation of a $2\sigma_u$ electron to states belonging to the Rydberg series of N_2 $nd\sigma_g$ $^1\Sigma_u^+$ and $nd\pi_g$ $^1\Pi_u$, respectively [22, 23]. Due to the coupling with the continuum, autoionization leads to the emission of an electron leaving the ion either in the $X^2\Sigma_g^+$ or in the $A^2\Pi_u$ state [24].

Between the ionization potential ($I_p = 15.58$ eV) and 16.8 eV (Fig. 2b central panel), the features are mainly attributed to two series of autoionizing resonances converging to the $A^2\Pi_u$ state [22].

Finally, below 15.6 eV (Fig. 2b lower panel) the absorption features are attributed to two series of excited states of the neutral molecule [24, 25], converging the ground ionic state $X^2\Sigma_g^+$, and to the first excited state $A^2\Pi_u$. Due to the finite energy resolution of the XUV spectrometer, the full structure of the excited states cannot be resolved.

The optical density was measured using broadband XUV continua generated in xenon by means of the polarization gating technique [26] and filtered using either indium or tin filters to obtain spectra centered around 15 eV (green line) and 18 eV (blue line), respectively (see Fig. 2a).

As can be observed in Fig. 2a,b, the Fano-resonances (blue shaded area in Fig. 2a and upper panel of Fig. 2b) and the states below (around) the ionization threshold (green shaded area in Fig. 2a and lower panel of Fig. 2b) are spaced by roughly 3 eV, corresponding to the energy of two IR photons. According to the simple three-state model, the coherent excitation of these electronic states due to the absorption of a single XUV photon and the subsequent interaction with a synchronized IR field, should lead to a coupling of the dipole moment and to a modulation of the absorption optical density. In this picture the bound excited states and the Fano resonances correspond to the states $|1\rangle$ and $|2\rangle$ of the three-state model shown in Fig. 1.

The possibility to change the spectrum of the XUV continua using different metallic filters, allows one to modify the initial population of the electronic wave packet. In particular, using a tin filter, it is possible to generate an XUV continuum centered

around 18 eV (blue spectrum in Fig. 2a), while using indium filter an XUV spectrum centered at 15 eV can be selected (green spectrum in Fig. 2a). Pulse durations of 927 as and 1.4 fs were retrieved using the FROG-CRAB algorithm for the two cases, respectively [27]. According to the mean photon energy of the XUV pulses, we will refer hereafter to the dynamics initiated by the two XUV spectra as low-energy excitation case (LEE) and high-energy excitation case (HEE), respectively. In the LEE case mainly the bound excited states of nitrogen are populated, whereas in the HEE case the two series of Fano resonances are efficiently excited. In both cases, the tail of the XUV spectra [towards the high (low) energies for the LEE (HEE) cases] creates a broadband electronic wave packet with components below and above the ionization threshold.

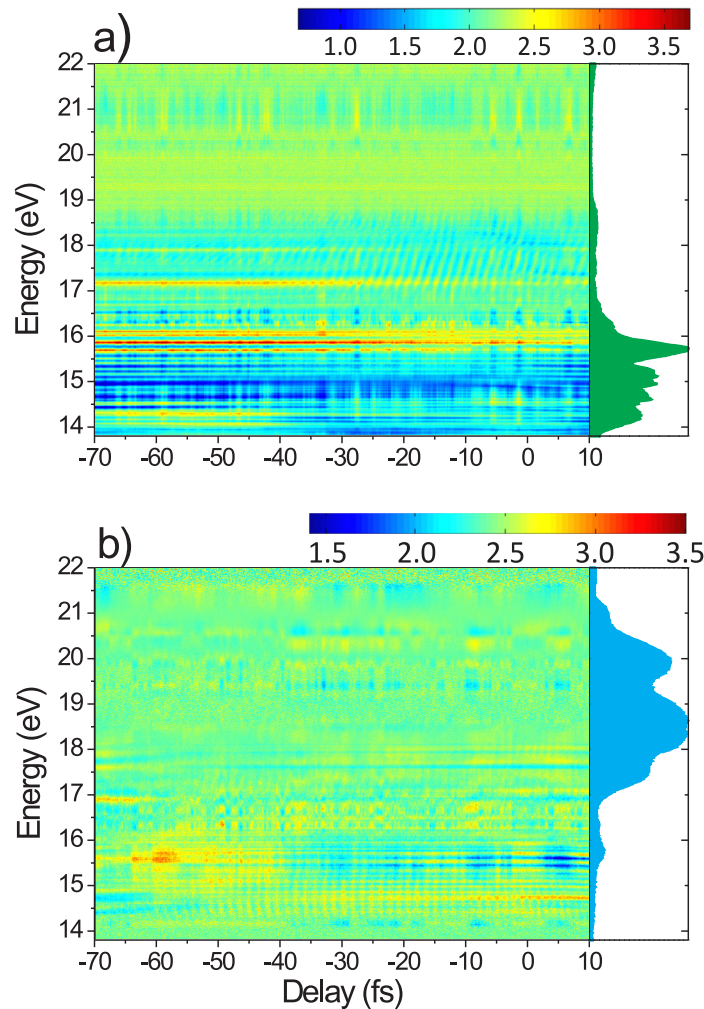


Figure 3. Optical densities as a function of the relative time delay between the IR and XUV pulses for the low-energy excitation (LEE) case (a) and the high-energy excitation (HEE) case (b). The excitation XUV spectra are shown on the right hand-side. The XUV field comes first for negative delays.

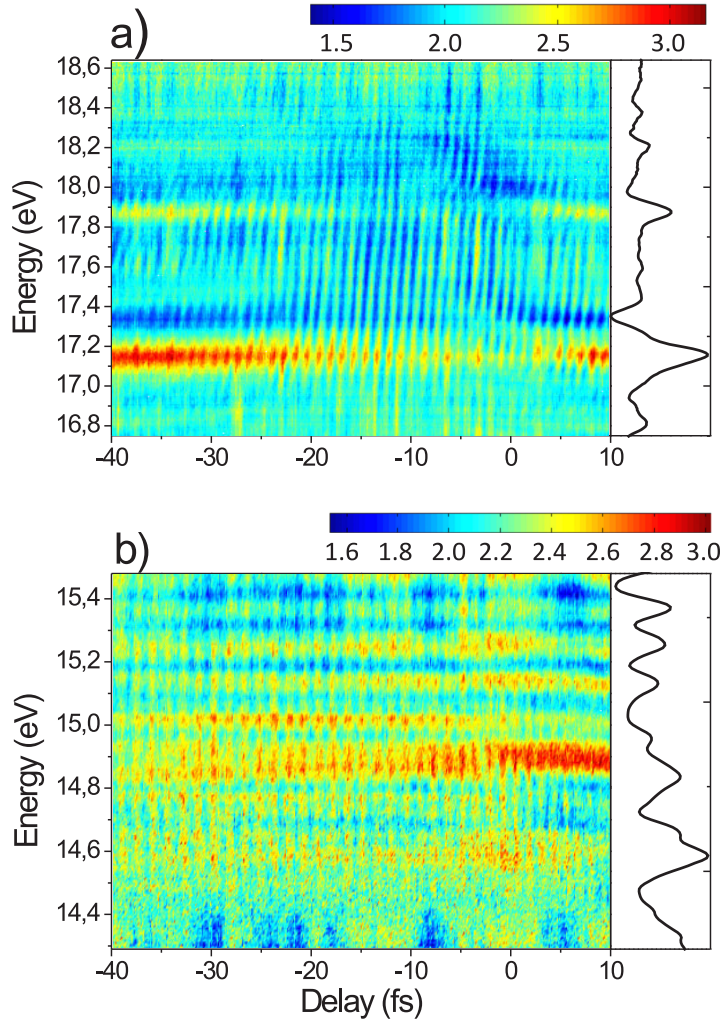


Figure 4. Enlarged view of the the optical density as a function of the relative delay between the IR and XUV pulses for the low-energy excitation LEE case in the region of the Fano resonances (a) and for the HEE case in the region of the bound states (b). The optical densities measured without IR pulse are shown on the right hand-side as references.

3. Sub-cycle quantum beating and autoionization dynamics

In the time-resolved experiments, a moderately intense ($I \simeq 10^{12}$ W/cm²) CEP-stabilized few-cycle IR pulse was introduced, with a variable time delay, to overlap with the XUV continua in the nitrogen cell. The optical density OD was measured as a function of the energy and of the relative time delay. The IR dressing pulse arrives after the XUV pulse for negative delays.

The delay-dependence of the optical density is shown in Figures 3a and 3b in the LEE and HEE cases with the corresponding XUV excitation spectrum (right hand-side), respectively. Clear oscillations with a period of $T = 1.3$ fs (corresponding to half-optical cycle of the IR field) are observed in particular energy ranges in both cases. It is important to point out that in the LEE case, the oscillations are evident for the Fano

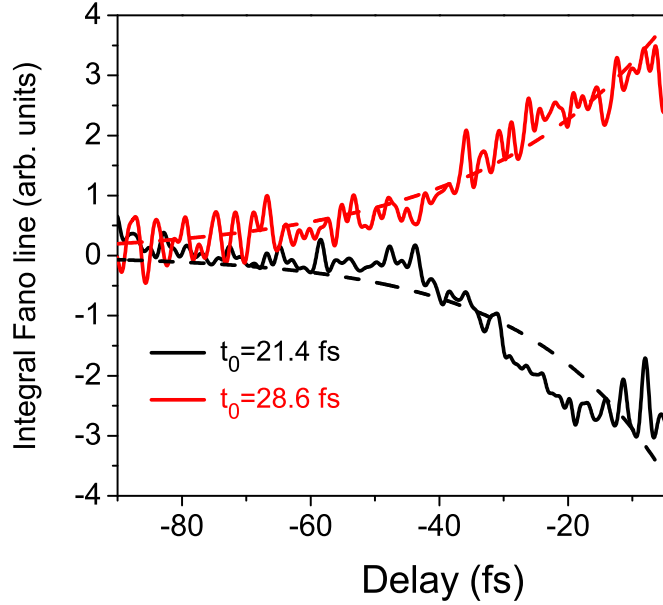


Figure 5. Integrated cross-section signal (solid line) around the Fano resonances $n=3$ of the series $nd\sigma_g \ ^1\Sigma_u^+$ (black) and $nd\pi_g \ ^1\Pi_u$ (red) (see Fig. 4a) as a function of the relative delay between the IR and XUV pulses. The values indicate the time constants t_0 of the two exponential fits (dashed lines).

resonances, i.e. in the energy region that is only weakly populated by the XUV radiation (see Figs. 3a and 4a); similarly, in the HEE case the oscillations are present only on the bound excited states (see Figs. 3b and 4b). As already anticipated the energy distance between these two groups of states is about 3 eV, indicating a two-photon coupling as origin of the observed modulation, in agreement with the simple three-state model described in the introduction. In Fig. 3b, half-cycle oscillation extending down to -60 fs can be observed. The origin of these oscillations can be attributed to a low intensity pedestal of the synchronized IR field. Indeed, even though pulses as short as 5.0 fs were characterized using the FROG technique, the different dispersion compensation between the point where the pulses are characterized and the nitrogen cell can lead to a low intensity pulse pedestal affecting the main pulse.

We point out that half-cycle oscillations were observed also using CEP unstable driving pulses, and trains of attosecond pulses. This observation indicates that the key element for the observation of the modulation of the optical density is the

synchronization between the attosecond pulses and the oscillation of the IR field. On the other hand, the possibility to (partially) shape and tune the XUV spectrum, allows one to enhance the modulation effect and to determine the spectral region where it is more evident. Because of the spectral distribution of the XUV pulses (as explained in the following), such oscillations are not present on the autoionizing states converging to the $A^2\Pi_u$ state. These states will not be discussed further in this work. We have experimentally verified that the contrast of the half-optical cycle oscillations strongly depends on the shape of the XUV spectra. In particular, the maximum contrast was achieved when the tails of the XUV spectral distributions were about 5%-10% of the main peak.

Beside the half-optical cycle oscillation in the signal, an overall depletion in the autoionizing region accompanied by broadening can be observed in Fig. 4a when the two pulses overlap and for short negative delays (the XUV field comes before the IR pulse), which indicates that the IR field ionizes these states before autoionization can occur. The level of depletion at each autoionizing state decreases at negative delays at half the rate of the decay lifetime of that state, and the signal revives at large negative delays. This type of time-domain measurement of autoionization has been performed in previous experiments [17, 28].

The lifetime $\tau = 1/\Gamma$ (where Γ indicates the linewidth of the autoionizing photoelectron line) of the first two Fano resonances can be retrieved from the experimental data by analyzing the delay-dependence of the integral of the Fano profile. In order to do this, we have first eliminated the oscillation at frequency 2ω by Fourier filtering and then integrated the optical density signal over the energy interval 17.0-17.25 eV and 17.25-17.45 eV corresponding to the $3d\sigma_g\ ^1\Sigma_u^+$ and $3d\pi_g\ ^1\Pi_u$ autoionizing states, respectively. The results are shown in Fig. 5. The exponential fits (dashed lines) indicate a time constant of $t_0 = 21.4$ fs and 28.6 fs, respectively. In the time domain, the decay dynamics of the integral signal is determined by the convolution of the cross-correlation of the excitation pulses (XUV and IR pulses) with the exponential decay of the polarization. The former one was estimated in $\simeq 8$ fs from the experimental rise (or decay) time of the signal at positive delays (see Fig. 5). We have verified that the decay constant of the polarization \bar{t} and the time constant t_0 are approximately given by $\bar{t} = 0.93 - 0.97t_0$, due to the non-zero cross-correlation. The lifetime τ of the autoionizing state is half the decay constant of the polarization \bar{t} [29], leading to $\tau=10.2$ fs and 13.8 fs for the $3d\sigma_g\ ^1\Sigma_u^+$ and $3d\pi_g\ ^1\Pi_u$ resonances, respectively.

These values should be compared to the measurement of the linewidth reported in literature: according to Gurtler and coworkers [24] the linewidth of the state $n=5$ of the series $nd\sigma_g\ ^1\Sigma_u^+$ is $\Gamma = 20$ meV corresponding to a lifetime $\tau = 32.9$ fs. Assuming a n^3 scaling (where n indicates the principal quantum number) for the lifetime of the autoionizing states [30], a decay constant $\tau = 7.1$ fs can be derived for the state $3d\sigma_g\ ^1\Sigma_u^+$ of the series. In ref. [30] the width of the state $n=3$ of the series $nd\sigma_g\ ^1\Sigma_u^+$ is about $\Gamma = 50.8$ meV corresponding to a decay constant $\tau = 12.9$ fs. We can therefore conclude that the measured decay time ($\tau=10.2$ fs) is intermediate and in reasonably

good agreement with previously reported experimental results.

4. Theoretical model and interpretation

The energy difference of about 3.1 eV between the two groups of levels suggests a two-photon (single photon energy $\hbar\omega \approx 1.55$ eV) coupling between the Fano resonances and the bound excited states, as origin of the half-optical cycle oscillations. We simulated the experimental results using the time-dependent perturbation (TDP) theory, which is valid if all transitions considered are weak in terms of transferred population. Two series of Fano resonances and two series of bound excited states were considered in the simulation, with the parameters extracted from the measured XUV spectra. To include IR ionization of the excited states, a decay rate for each state as a function of the IR intensity was introduced. The rate was estimated with general approximations regarding the coupling of autoionizing states by ultrashort pulses and the associated light absorption [31]. The XUV pulse creates a broadband electronic wave packet composed by the ground state $|g\rangle$, the bound states $|b_m\rangle$ below the ionization threshold I_p and the autoionizing states $|f_n\rangle$ embedded in the background continuum $|E\rangle$ above I_p . The general total wave function of the system is (atomic units are used unless otherwise specified)

$$|\Psi(t)\rangle = e^{-iE_g t} c_g(t) |g\rangle + e^{-i(E_g + \omega_X)t} \left[\sum_m c_m(t) |b_m\rangle + \sum_n c_n(t) |f_n\rangle + \int c_E(t) |E\rangle \right]. \quad (3)$$

Here the fast oscillating terms are factored out where E_g and ω_X are the ground state energy and the XUV carrier frequency, respectively, and all the $c(t)$ coefficients of states near the XUV energy are smooth in time. The indices m and n are used exclusively for the bound states and Fano resonances, respectively. The XUV spectral distributions mimic the experimental one, leading to a much more efficient population of the $|b_m\rangle$ or $|f_n\rangle$ states in the LEE and HEE case, respectively (see Fig. 6a). Meanwhile the IR pulse ($\lambda = 780$ nm and FWHM=5 fs) couples the two groups of states separated by two IR photon energies. The product of the IR intensity and the overall dipole matrix element is adjusted to maximize the oscillation contrast. Because of the significant imbalance of populations, the IR mainly transfers the electrons from the highly populated group to the weakly occupied group, i.e., either from $|b_m\rangle$ to $|f_n\rangle$ or from $|f_n\rangle$ to $|b_m\rangle$. In the LEE case, the final $|f_n\rangle$ states, while weakly populated, consist of the electrons from the direct XUV excitation and from the XUV+2IR three-photon excitation through the $|b_m\rangle$ states. Thus, the spectrum around $|f_n\rangle$ shows the interference pattern formed by the two paths. Similarly, in the HEE case, where XUV concentrates on $|f_n\rangle$, the interference pattern is observed around $|b_m\rangle$. In this model the IR transition brings just equivalently small amount of population to the weakly pumped states. The XUV photon energy is assumed to be much higher than its bandwidth. We apply rotating wave approximation and slowly varying envelope and write the XUV electric field in the

general form of

$$E_X(t) = F_X(t)e^{i\omega_X t} + F_X^*(t)e^{-i\omega_X t}, \quad (4)$$

where $|2F_X(t)|^2$ is the intensity profile of the pulse, and $F_X(t)$ contains any phase information additional to the carrier frequency. Focusing on the LEE case first, taking the time derivative form of TDP, the coefficients of the autoionizing states $|f_n\rangle$ are calculated by

$$\dot{c}_n(t) = i\bar{D}_{ng}F_X^*(t) - \sum_m D_{nm}E_L^2(t)c_m^{(0)}(t) + [i\delta_n - \kappa_n - w_n(t)]c_n(t). \quad (5)$$

The first term is the contribution by the XUV transition from the ground state, where the ground state coefficient is assumed to remain 1. The complex dipole matrix elements $\bar{D}_{ng} \equiv D_{ng}(1 - i/q_n)$ are between $|g\rangle$ and the Fano resonances at $|f_n\rangle$, which contain the Fano q parameters and encode the Fano line shapes in the coefficients $c_n(t)$. The second term is the contribution by the two-photon IR transition from all the $|b_m\rangle$ states, where the dipole matrix elements D_{nm} represent the two-photon transition matrix summing over all intermediate states, assuming none of them is resonant [32]. The coefficients $c_m^{(0)}(t)$ are prepared by solving

$$\dot{c}_m^{(0)}(t) = iD_{mg}F_X^*(t) + [i\delta_m - \kappa_m - w_m(t)]c_m^{(0)}(t). \quad (6)$$

In the last term on the right hand side of Eq. (5), $\delta_n \equiv E_g + \omega_X - E_n$ is the detuning of the XUV with respect to state $|f_n\rangle$, and $\Gamma_n \equiv 2\kappa_n \equiv 2\pi V_n^2$ and $2w_n(t)$ are the resonance width and IR ionization rate of $|f_n\rangle$. Note that the δ_m and δ_n in Eqs. (5) and (6) do not appear in the common TDP formulas written in Dirac picture because the phase terms of the excited states in our total wave function are defined relative to the XUV central frequency but not to the state energy levels. The IR ionization rates $w_n(t)$ and $w_m(t)$ are assumed to be proportional to the IR intensity because these states are close to the ionization threshold in terms of the IR photon energy, and single photon or multiphoton ionization instead of tunnel ionization more suitably describes the process. The actual rates are estimated by fitting with the present experimental data. For the HEE case, similar procedure described above is taken. The coefficients of $|b_m\rangle$ are calculated by

$$\dot{c}_m(t) = iD_{mg}F_X^*(t) - \sum_n D_{mn}E_L^2(t)c_n^{(0)}(t) + [i\delta_m - \kappa_m - w_m(t)]c_m(t), \quad (7)$$

where $c_n^{(0)}(t)$ are given by

$$\dot{c}_n^{(0)}(t) = i\bar{D}_{ng}F_X^*(t) + [i\delta_n - \kappa_n - w_n(t)]c_n^{(0)}(t). \quad (8)$$

Here we obtain the total wave function beside the background continuum for any given set of XUV and IR pulses and parameters. The exact calculation for the continuum part is not necessary for the absorption spectrum as will be shown later.

It is to be emphasized that all optical transitions in the current model are based on TDP, so each transition is weak and has only one direction, from the highly populated state (as the initial state) to the weakly populated state (as the final state). The conservation of electronic probability (or of energy) does not apply because the initial

state is not changed by the transition. The strong coupling involving Rabi flopping or involving dressed states is excluded in this model. Thus, many features observed in the strongly coupled transient absorption experiments [18, 19] cannot be recovered here.

To determine the input atomic parameters, the experimental data were analyzed. The line widths of the lowest two autoionizing states at 17.15 and 17.32 eV are extracted from the signal along the resonances in the time-delayed XUV absorption measurement (the spectral resolution of the XUV spectrometer was taken into account). The q parameters of the same two states are extracted from the field-free XUV absorption spectroscopy. These two states are the most easily observed states belonging to the two series that we consider. The widths of higher resonances can be estimated by the quantum defect rule $\Gamma\nu^3 = \text{const.}$ for each series [30], where ν are the effective quantum numbers, which can be approximated by the principal quantum numbers n for low angular momentum. The q parameter for each series is assumed to be constant. The parameters for the autoionizing states are listed in Table 1. The

Table 1. Parameters of the autoionizing states used in the main simulation.

n	$E_r(\text{eV})$	$\Gamma(\text{meV})$	q
3	17.15	30.8	-3.0
3	17.32	23.0	-0.5
4	17.84	13.0	-3.0
4	17.94	9.7	-0.5
5	18.18	6.7	-3.0
5	18.23	5.0	-0.5
6	18.37	3.9	-3.0

energy levels and line widths of the bound states $2\kappa_m$ are extracted from the field-free XUV absorption measurement and listed in Table 2. The relative strengths of the dipole matrix elements between the bound excited states and the autoionizing states are assumed to be proportional to $V_m V_n$. The overall strength between the group of bound excited states and the group of autoionizing states is adjusted to maximize the contrast of the interference fringes in the main result. The light absorption of the system corresponds to its dipole oscillation in time $D(t) = \langle \Psi(t) | D | \Psi(t) \rangle$. The XUV absorption thus corresponds to the oscillation in the XUV frequency range, which for the total wave function in Eq. (3) can be reduced to [31]

$$D(t) = e^{i\omega_X t} \left[\sum_m \bar{D}_{gm} c_m^*(t) + \sum_n D_{gn} c_n^*(t) - i\pi F_X(t) |D_{gE}|^2 \right] + c.c., \quad (9)$$

where we have assumed $c_g(t) = 1$ and taken the approximation where D_{gE} is constant of E estimated at the lowest f_m . Note that for each Fano resonance, a given set of constant D_{gE} , resonance width Γ_n , and $q_n \equiv D_{gn}/(\pi V_n D_{gE})$ determines the dipole matrix element D_{gn} . Further details for autoionizing systems coupled by an ultrashort intense laser have been discussed in Ref. [31]. The present observed experimental features are from the

Table 2. Parameters of the bound excited states used in the main simulation. The line shapes are assumed Lorentzian.

E_r (eV)	Γ (meV)
13.98	0.02
14.07	0.02
14.14	0.02
14.22	0.02
14.28	0.02
14.50	0.02
14.59	0.02
14.72	0.02
14.85	0.02
15.03	0.02
15.14	0.02
15.23	0.02
15.36	0.02
15.48	0.02

interference between the two paths introduced above, where only their relative but not absolute strengths are essential, and each path is formed by the dipole matrix elements coupled with the field strength. The absorption of the XUV light is obtained through the response function [33] given by

$$S(\omega) = -2\text{Im} \left[\tilde{D}(\omega) \tilde{E}_X^*(\omega) \right], \quad (10)$$

which represents the absorption probability density in frequency, where the convention for Fourier transform is

$$\tilde{f}(\omega) = \frac{1}{\sqrt{2\pi}} \int e^{-i\omega t} f(t) dt. \quad (11)$$

The absorption cross section $\sigma(\omega)$ in the XUV energy range, which is proportional to the optical density $\text{OD}(\omega)$ reported in the experiment, is related to the response function by

$$\sigma(\omega) = \frac{4\pi\alpha\omega S(\omega)}{|\tilde{E}_X(\omega)|^2}, \quad (12)$$

where α is the fine structure constant.

The simulated cross section is reported in Fig. 6a (green line) with the corresponding XUV spectra of the attosecond pulses used in the simulations. In order to compare the outcome of the simulations with the experimental data, the resolution of the XUV spectrometer was included, by convoluting the simulated cross section with a gaussian function, whose width corresponds to the spectral resolution (black line in Fig. 6a). The simulations, shown in Fig. 6b and 6c, clearly reproduce the periodic oscillations and the IR-induced depletion and broadening of the time-delayed signals in both the

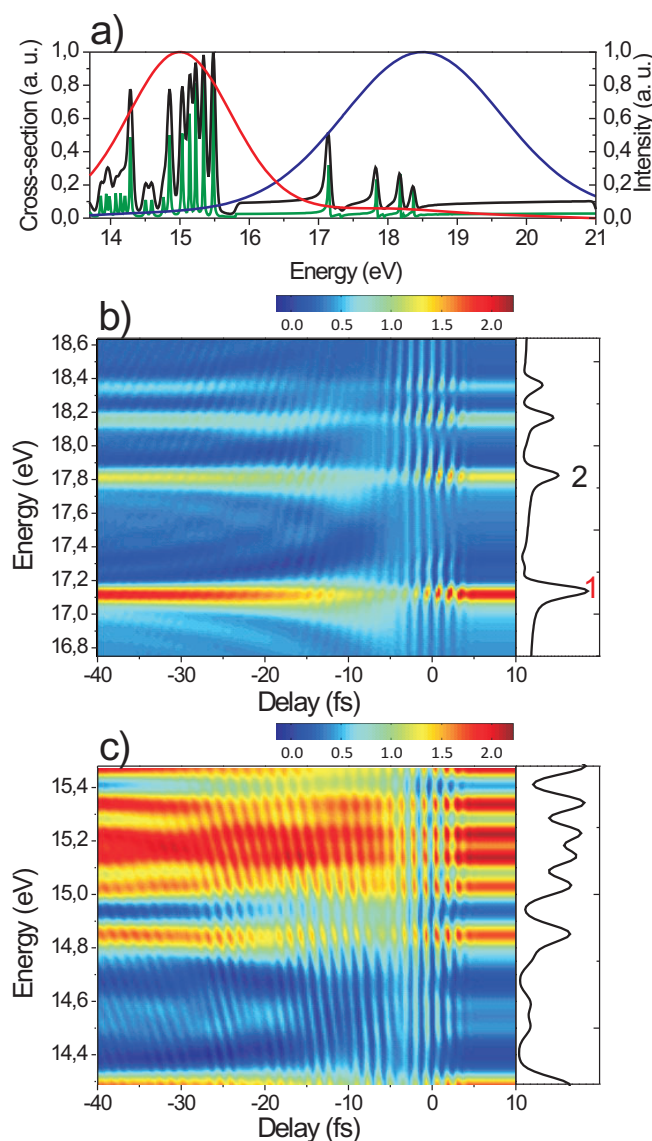


Figure 6. a) Simulated cross-section in nitrogen using experimental data without (green line) and with convolution (black line) with the limited experimental spectral resolution (left axis). Simulated XUV spectral distributions for the LEE (red curve) and HEE (blue curve) cases. b) LEE: simulated cross-section as a function of the relative delay between the IR and XUV pulses in the spectral region of the Fano-Beutler resonances. The convoluted cross-section is shown on the right hand-side for reference. c) HEE: simulated cross-section as a function of the relative delay between the IR and XUV pulses in the spectral region corresponding to the bound excited states. The convoluted cross-section is shown on the right hand-side for reference. The two-dimensional cross-sections have been convoluted with the spectral response of the XUV spectrometer.

LEE and the HEE cases, in agreement with the experimental results. The presence of these oscillations supports the conclusion of an IR-coupling occurring between the two groups of states. The slopes of the oscillation fringes also fit the experiment well. The simulations allow to conclude that in the LEE (HEE) case, when the XUV light pumps

effectively the bound states (Fano resonances), the amplitudes of the Fano resonances (bound states) are the result of the coherent sum of the weak direct XUV-excitation path (due to the tail of the XUV spectrum) and the XUV+2IR photons excitation mechanism through the bound states (Fano resonances).

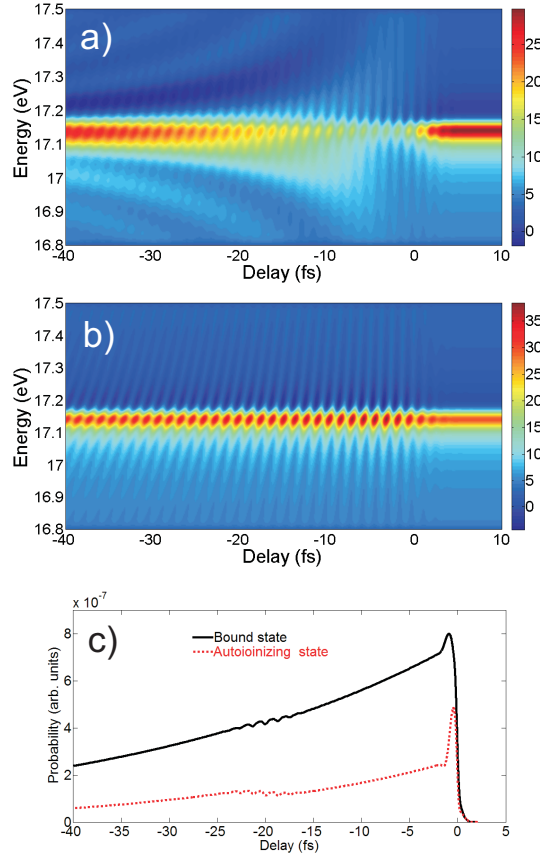


Figure 7. Simulated delay-dependent cross section near the lowest Fano resonance in the three-level system (ground state, bound state at 13.98 eV, and Fano resonance at 17.15 eV.) in the LEE case, (a) with and (b) without the ionization by the IR pulse. (c) The probabilities of the bound state and the autoionizing state evolving in time where the XUV peak is at $t = 0$ fs and the IR peak is at $t = -20$ fs, without the IR ionization.

In order to support this main conclusion, we conducted a simulation with the same field parameters of the LEE case but in a reduced system composed by only three quantum levels—the ground state, the bound excited state at 13.98 eV, and the Fano resonance at 17.15 eV. The two excited levels are separated energetically by two IR photons. As seen in Fig. 7a, the half-optical-cycle oscillation and the time-dependent depletion are reproduced very well. It confirms that the main features shown in the experiment are already manifested by the coupling in a simple three-level system. Nonetheless, there still exist some noticeable differences from the full simulation. For instance, the spectral span near the zero time delay is narrower, and the nearly vertical fringes shrink to only short pieces at the resonance. Furthermore, the overall signal

strength is weaker, which brings down the sharpness and the contrast of the interference pattern as well. It shows that the interference effect in our experiment is the collective contribution by all the direct (XUV) and indirect (XUV+2IR) excitations.

When we further remove the IR ionization (Fig. 7b), the shift of the slope of the half-optical-cycle fringes becomes very regular along the time delay, which has been demonstrated in photoelectron spectroscopy theoretically [34] and experimentally [35]. In the time domain, Fig. 7c shows the populations of the two excited states, where the peak of IR is 20 fs later than the peak of XUV (0 fs). After being pumped by the XUV, both excited states drop exponentially with their respective decay lifetimes. At $t=-20$ fs, the interaction with the IR pulse redistributes the components of the wave packet, and the autoionizing state receives a jump in the population. These simulations confirm the simple physical picture outlined in section 2.

The energy position of the interference fringes is determined by the initial population of the electronic wave packet components as shown in Figs. 8a, which reports the Fourier transform along the delay axis of the energy-delay scan for the LEE case (Fig. 3b). The half-cycle oscillations as a function of the delay correspond to the features visible at energies $\omega' = 2\omega_{IR}$ (≈ 3.1 eV) around the Fano resonances (17.0-18.6 eV). The situation reverses for the HEE case, where features around $\omega' = 2\omega_{IR}$ are visible around the energies of the bound states (14.5-15 eV) (not shown). In both cases, the group of states that is more effectively populated by the XUV pulse present a much reduced oscillation with respect to the other one. This observation points out that the cross-section modulations can be observed only if the two interfering paths present similar contributions to the total cross-section. For the group of state directly populated by single-XUV-photon absorption, the second path, characterized by XUV+2IR photons, is too weak to produce a clear interference and a measurable cross-section oscillation. Therefore, the spectrum of the attosecond pulse determines which group of states will present the most pronounced absorption modulation due to the two-photon coupling. A closer look at the LEE case (Fig. 8b) reveals that the signal at $2\omega_{IR}$ is characterized by a series of tilted lines oriented at 45 degree in the (ω, ω') plane. The Fourier analysis of the simulations (see Fig. 8c) shows a similar qualitative behavior confirming the presence of these lines around the position $\omega' = 2\omega_{IR}$. Each of these feature is associated to a XUV+2IR path through a single bound excited state. Exploiting the beating between different components of the electronic wave packet, we can dynamically enhance with an attosecond time resolution the population of the Fano resonances in the LEE case and of the bound excited states in the HEE case. This control is directly mapped in the delay dependence of the cross-section as shown in Fig. 8d, which reports the final population (i.e. after the interaction with both pulses) of the two Fano resonances (states indicated by 1 and 2 in Fig. 6b) and the corresponding cross-section as a function of the relative delay between the XUV and IR pulses. The relative delays between -30 to -20 fs ensure that the IR control field arrives well after the initial excitation of the XUV pulse. The oscillation of the population of the excited states are directly mapped on the modulation

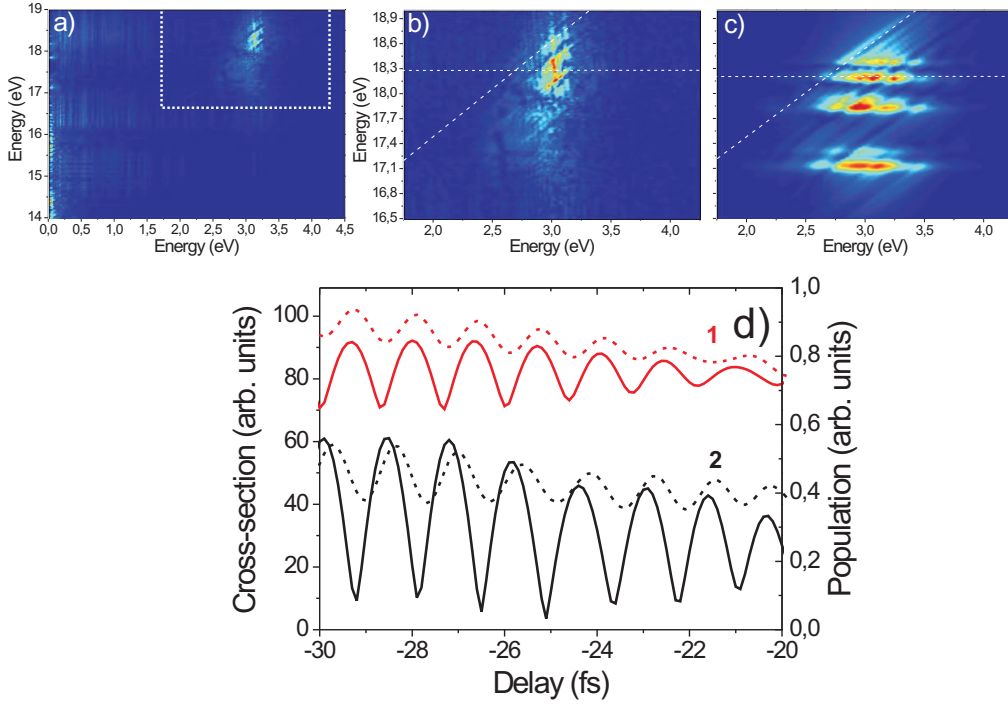


Figure 8. (a) Fourier transform of the delay-dependent cross-section shown in Fig. 3b (LEE case). (b) Enlarged view of the region around $\omega = 17.5$ eV and $\omega' = 3.1$ eV delimited by dashed lines in (a). (c) Fourier analysis of the simulated delay-dependent cross-section shown in Fig. 6b. The dotted white lines are guides for the eyes. (d) Simulated delay-dependence of the final population (solid lines) and of the cross-section (dashed lines) for the Fano-resonance with energy 17.1 eV (1; red), and with energy 17.8 eV (2; black), shown in Fig. 6b. The curves have been vertically displaced for visual clarity.

of the transmitted XUV spectrum, thus allowing a straightforward visualization of the variations of the electronic wave packet induced by the IR field.

5. Conclusions

In conclusion, we have investigated the ultrafast electronic dynamics occurring in a nitrogen molecule excited by a tunable XUV continuum. The decay time of two Fano resonances can be retrieved exploiting the ionization induced by a few-cycle IR field. At the same time, the IR pulse perturbs the coherent dipole oscillations inducing modulations in the transmitted XUV radiation, which are sensitive to the relative amplitude and relative phase of the components of the electronic wave packet. The energy range where such modulations are enhanced can be controlled by manipulating the initial state population. The use of tunable IR/visible fields or temporally shaped pulses might allow the investigation of the spectrally and temporally resolved beating of selected components of a broadband wave packet. By combining spectral and phase characterization of the transmitted XUV field, it will be possible to infer additional

information about the time evolution of the electronic wave packet with the aid of theoretical modeling.

6. Acknowledgments

Financial support by the Alexander von Humboldt Foundation (Project “Tirinto”), the Italian Ministry of Research (Project FIRB No. RBID08CRXK), the European Research Council under the European Communitys Seventh Framework Programme (FP7/2007-2013) / ERC grant agreement n. 227355 - ELYCHE, the MC-RTN ATTOFEL (FP7-238362) ATTOFEL, LASERLAB-EUROPE (grant agreement n. 284464, EC’s Seventh Framework Programme), and Chemical Sciences, Geosciences and Biosciences Division, Office of Basic Energy Sciences, Office of Science, U. S. Department of Energy, is gratefully acknowledged. This project has received also funding from the European Union’s Horizon 2020 research and innovation programme under the Marie Skłodowska-Curie grant agreement no. 641789 MEDEA. The authors also want to thank C. Ott for fruitful discussions.

References

- [1] Krausz F. and Ivanov M. 2009 *Rev. Mod. Phys.* 81 163–234.
- [2] Corkum P. B. and Krausz F. 2007 *Nature Phys.* 3 381–87.
- [3] Nisoli M. and Sansone G. 2009 *Progr. Quantum Electron.* 33 17–59.
- [4] Lépine F., Sansone G., and Vrakking M. J. J. 2013 *Chem. Phys. Lett.* 578 1–14.
- [5] Kapteyn H., Cohen O., Christov I., and Murnane M. 2007 *Science* 317 775–78.
- [6] Mauritsson J., Remetter T., Swoboda M., Klunder K., L’Huillier A., Schafer K. J., Ghafur O., Kelkensberg F., Siu W., Johnsson P., Vrakking M. J. J., Znakovskaya I., Uphues T., Zherebtsov S., Kling M. F., Lépine F., Benedetti E., Ferrari F., Sansone G., and Nisoli M. 2010 *Phys. Rev. Lett.* 105 053001.
- [7] Breidbach J. and Cederbaum L. S. 2005 *Phys. Rev. Lett.* 94 033901.
- [8] Remele F. and Levine R. D. 2006 *Proc. Natl. Acad. Sci. USA* 103 6793–98.
- [9] Cederbaum L. S. 2008 *J. Chem. Phys.* 128 124101.
- [10] Sansone G., Kelkensberg F., Perez-Torres J. F., Morales F., Kling M. F., Siu W., Ghafur O., Johnsson P., Swoboda M., Benedetti E., Ferrari F., Lépine F., Sanz-Vicario J. L., Zherebtsov S., Znakovskaya I., L’Huillier A., Ivanov M. Y., Nisoli M., Martin F., and Vrakking M. J. J. 2010 *Nature* 465 763–66.
- [11] Neidel C., Klei J., Yang C. H., Rouzee A., Vrakking M. J. J., Klunder K., Miranda M., Arnold C. L., Fordell T., L’Huillier A., Gisselbrecht M., Johnsson P., Dinh M. P., Suraud E., Reinhard P. G., Despre V., Marques M. A. L., and Lépine F. 2013 *Phys. Rev. Lett.* 111 033001.
- [12] Chen S. H., Bell M. J., Beck A. R., Mashiko H., Wu M. X., Pfeiffer A. N., Gaarde M. B., Neumark D. M., Leone S. R., and Schafer K. J. 2012 *Phys. Rev. A* 86 063408.
- [13] Chini M., Wang X. W., Cheng Y., Wu Y., Zhao D., Telnov D. A., Chu S. I., and Chang Z. H. 2013 *Sci. Rep.* 3 1105.
- [14] Holler M., Schapper F., Gallmann L., and Keller U. 2011 *Phys. Rev. Lett.* 106 123601.
- [15] Lucchini M., Herrmann J., Ludwig A., Locher R., Sabbar M., Gallmann L., and Keller U. 2013 *New J. Phys.* 15 103010.
- [16] Wang X. W., Chini M., Cheng Y., Wu Y., Tong X. M., and Chang Z. H. 2013 *Phys. Rev. A* 87 063413.

- [17] Wang H., Chini M., Chen S. Y., Zhang C. H., He F., Cheng Y., Wu Y., Thumm U., and Chang Z. H. 2010 *Phys. Rev. Lett.* 105 143002.
- [18] Loh Z. H., Greene C. H., and Leone S. R. 2008 *Chem. Phys.* 350 7–13.
- [19] Ott C., Kaldun A., Argenti L., Raith P., Meyer K., Laux M., Zhang Y. Z., Blattermann A., Hagstotz S., Ding T., Heck R., J. Madronero, Martin F., and Pfeifer T. 2014 *Nature* 516 374–378.
- [20] Ott C., Kaldun A., Raith P., Meyer K., Laux M., Evers J., Keitel C. H., Greene C. H., and Pfeifer T. 2013 *Science* 340 716–20.
- [21] Hopfield John J. 1930 *Phys. Rev.* 35 1133–34.
- [22] Berg L. E., Erman P., Kallne E., Sorensen S., and Sundstrom G. 1991 *Phys. Scripta* 44 131–37.
- [23] Raoult M., Rouzo H. Le, Raseev G., and Lefebvre-Brion H. 1983 *J. Phys. B* 16 4601.
- [24] Gürtler P., Saile V., and Koch E. E. 1977 *Chem. Phys. Lett.* 48 245–50.
- [25] Huffmann R.E., Y.Tanaka, and Larrabee J.C. 1963 *J. Chem. Phys.* 39 910.
- [26] Sansone G., Benedetti E., Calegari F., Vozzi C., Avaldi L., Flammini R., Poletto L., Villoresi P., Altucci C., Velotta R., Stagira S., De Silvestri S., and Nisoli M. 2006 *Science* 314 443–46.
- [27] Mairesse Y. and Quéré F. 2005 *Phys. Rev. A* 71 011401.
- [28] Gilbertson S., Chini M., Feng X. M., Khan S., Wu Y., and Chang Z. H. 2010 *Phys. Rev. Lett.* 105 263003.
- [29] Bernhardt B., Beck A. R., Li X., Warrick E. R., Bell M. J., Haxton D. J., McCurdy C. W., Neumark D. M., and Leone S. R. 2014 *Phys. Rev. A* 89 023408.
- [30] Huber K. P., Stark G., and Ito K. 1993 *J. Chem. Phys.* 98 4471–4477.
- [31] Chu W. C. and Lin C. D. 2013 *Phys. Rev. A* 87 013415.
- [32] Meshulach D. and Silberberg Y. 1999 *Phys. Rev. A* 60 1287–92.
- [33] Gaarde M. B., Buth C., Tate J. L., and Schafer K. J. 2011 *Phys. Rev. A* 83 013419.
- [34] Choi N. N., Jiang T. F., Morishita T., Lee M. H., and Lin C. D. 2010 *Phys. Rev. A* 82 013409.
- [35] Kim K. T., Ko D. H., Park J., Choi N. N., Kim C. M., Ishikawa K. L., Lee J., and Nam C. H. 2012 *Phys. Rev. Lett.* 108.